PAPER
Kuo-Yu Chen, Chih-Feng Huang *et al.*
Effects of various Cu(0), Fe(0), and proanthocyanidin reducing agents on Fe(III)-catalysed ATRP for the synthesis of PMMA block copolymers and their self-assembly behaviours

PAPER

Check for updates

Effects of various Cu(0), Fe(0), and proanthocyanidin reducing agents on Fe(III)-catalysed ATRP for the synthesis of PMMA block copolymers and their self-assembly behaviours†

Yi-Shen Huang,‡[a] Han-Yu Hsueh,‡[b] Junko Aimi, [ID][c] Li-Chieh Chou, [ID][a] Yu-Chi Lu,[a] Shiao-Wei Kuo, [ID][d,e] Chung-Chi Wang,[f] Kuo-Yu Chen*[g] and Chih-Feng Huang [ID]*[a]

We applied environmentally friendly ferric complexes (*i.e.*, FeCl₃/PPh₃) to one of the most widely-used controlled/living polymerizations (CRP), atom transfer radical polymerisation (ATRP), for the preparation of well-defined poly(methyl methacrylate) (PMMA) homo- and block (co)polymers. Iron-catalysed supplemental activator and reducing agent (SARA) and activators regenerated by electron transfer (ARGET) ATRPs were investigated using cost-effective Cu(0), Fe(0), and the natural antioxidant proanthocyanidins (PC) as reducing agents. With different ratios of Fe(III)/Cu(0) and Fe(III)/Fe(0) for ATRPs of MMA, the former exhibited fast apparent reaction rates (k_{app}s >3 × 10⁻⁵ s⁻¹), but showed large PDI values (>1.6); the latter exhibited moderate k_{app}s (= *ca.* 7 × 10⁻⁶–3 × 10⁻⁵ s⁻¹) with low PDI values (<1.45), indicating that moderate reactions could avoid the occurrence of undesired side reactions. In the case of Fe(III)/PC, interestingly, moderate k_{app}s (= *ca.* 3 × 10⁻⁶–8 × 10⁻⁶ s⁻¹) with low PDI values (<1.30) were obtained. Through UV–Vis measurements and additional chain extension of MMA, the effective reduction of PC on Fe(III) was obviously observed and resulted in high chain functionality of the PMMA–Br macroinitiator. Subsequently, two more chain extensions of PMMA–Br with *n*-butyl methacrylate (BMA) and benzyl methacrylate (BzMA) were conducted to obtain well-defined PMMA₁₀₀-*b*-PBMA₅₃₇ ($M_{n,NMR}$ = 86 300; PDI = 1.25) and PMMA₁₀₀-*b*-PBzMA₆₄₉ ($M_{n,NMR}$ = 124 200; PDI = 1.35) block copolymers (BCPs). Their thermal properties were characterized by thermogravimetric analysis (TGA) and differential scanning calorimetry (DSC). The segmental segregation was characterized by small-angle X-ray scattering (SAXS) and atomic force microscopy (AFM). Interestingly, microphase separation was observed only in the PMMA₁₀₀-*b*-PBMA₅₃₇ BCP with an upper critical ordering temperature (UCOT) behaviour and acquired spherical nanostructure (*d* = *ca.* 25 nm). We thus demonstrate a "green" ATRP method mainly using the natural product PC to reduce the FeCl₃/PPh₃ complex for the preparation of well-defined polymethacrylate-based BCPs.

[a]*Department of Chemical Engineering, i-Center for Advanced Science and Technology (iCAST), National Chung Hsing University, 145 Xingda Road, South District, Taichung 40227, Taiwan. E-mail: HuangCF@dragon.nchu.edu.tw*
[b]*Department of Materials Science and Engineering, National Chung Hsing University, Taichung 40227, Taiwan*
[c]*Molecular Design & Function Group, Research Center for Functional Materials, National Institute for Materials Science, 1-2-1 Sengen, Tsukuba, Ibaraki 305-0047, Japan*
[d]*Department of Materials and Optoelectronic Science, Center of Crystal Research, National Sun Yat-Sen University, Kaohsiung 80424, Taiwan*
[e]*Department of Medicinal and Applied Chemistry, Kaohsiung Medical University, Kaohsiung 80708, Taiwan*
[f]*Division of Cardiovascular Surgery, Veterans General Hospital, Taichung, Taiwan*
[g]*Department of Chemical and Materials Engineering, National Yunlin University of Science and Technology, Yunlin 64002, Taiwan. E-mail: chenkuo@yuntech.edu.tw*
†Electronic supplementary information (ESI) available. See DOI: 10.1039/d0py00658k
‡These authors contributed equally to this work as first authors.

1. Introduction

With the robust methods of controlled/living polymerization (CRP), various monomers can be tailor-made to well-defined polymers with a predictable molecular weight (MW) and low polydispersity index (PDI) in a cost-effective manner. The most popular CRPs include atom transfer radical polymerization (ATRP),[1,2] reversible addition–fragmentation chain transfer (RAFT) polymerization,[3–5] and nitroxide-mediated radical polymerization (NMP).[6] Among them, ATRP serves as one of the most powerful platforms to obtain specific macromolecules,[7–9] including functional linear/branched polymers, periodic copolymers, and block copolymers (BCPs), as well as surface modifications.[10,11] The development of "green" ATRP is thus always on demand and much effort has been made for its practical applications.

ATRP techniques have been demonstrated their regulating effectiveness on the basis of systematic studies on the structural influences of initiators, transition metals, ligands, and solvents[12,13] as well as regulations *via* external stimuli. However, some of the effective metal complexes might be fatal or result in coloured products that are generally unwanted for practical usage. Several interesting and innovative ATRPs are conducted through external electrochemical (*i.e.*, *e*ATRP),[14–16] photochemical (*i.e.*, photo-ATRP),[17–19] mechanical (*i.e.*, mechano-ATRP),[20,21] or ultrasonic (*i.e.*, sono-ATRP) stimuli.[22,23] These reactions provide alternative reaction setups that can facilely suppress the amounts of undesirable colour, byproducts, or impurities. In addition, most of the typical approaches toward "green" ATRPs are to decrease the amount of transition metal catalysts (down to a parts-per-million (ppm) level). Such diminishing catalyst techniques, including activators regenerated by electron transfer (ARGET),[24,25] initiators for continuous activator regeneration (ICAR),[26] and supplemental activator and reducing agent (SARA)[27] ATRPs as well as the aforementioned *e*ATRP[14–16] and photo-ATRP,[28,29] generally proceed with the aid of excess amounts of reducing agents (RAs) (*e.g.*, ascorbic acid,[30–34] zero-valent metals,[27,35] azo compounds,[36–39] and others[40–43]). Among RAs, the use of natural products (*e.g.*, Vitamin C) is still limited as an effective reducing agent for ATRP with diminishing catalysts. Furthermore, iron-based complexes were regarded as one of the best choices for "green" reaction due to their low toxicity, cost-effectiveness, and environmentally friendly properties compared to other transition metal catalysts.[44,45] Therefore, combinations of iron catalysts and natural reducing agents could provide a highly "green" ATRP system.

Using CRPs and their orthogonal combinations,[46–49] we can facilely obtain various well-defined BCPs that show interesting and fascinating self-assembly behaviors in the solid- and solution-state for the preparation of nanostructural materials.[50] Through the manipulation of the microphase morphology of BCPs and/or their hybridizations, the affiliating applications include plastic/elastomer toughening, lithographic patterning, ion battery electrolyte support, and electronics fabrication. Typical morphologies of BCP self-assemblies mainly cover body-centered cubic (BCC) spheres, hexagonally close-packed cylinders (HPC), connected triply periodic gyroid (Gyd) networks, and lamellae (Lam). Recently, an extraordinary rare A15 microphase self-assembled from BCPs with an additive was discovered.[51] The A15 microphase is an analogue of low-symmetry sphere phases exhibiting tetrahedral close-packing and it could thus enlarge the application window of BCPs. Thus "green" ATRPs of ubiquitous monomers to synthesize well-defined BCPs provide a practical access for the preparation of interesting microdomains.

In this study, we employ diminishing amounts of iron catalysts to conduct ATRPs of methacrylate monomers in the presence of various reducing agents (RAs). We attempt to provide a practical access based on its low cost and environmentally friendly features. As shown in Scheme 1, we utilize a higher-oxidation-state ferric catalyst (*i.e.*, FeCl$_3$) with excess amounts
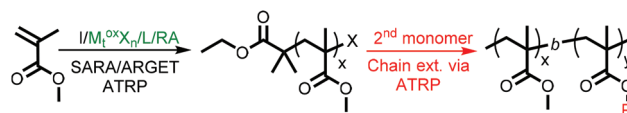
Scheme 1 "Green" ATRP using higher oxidation state metal compounds reduced by Cu(0), Fe(0), and proanthocyanidins for the synthesis of polymethacrylate-based block copolymers.

of RAs based on the mechanism of SARA or ARGET ATRP. We subsequently conduct chain extensions to synthesize well-defined polymethacrylate-based BCPs and observe their preliminary self-assembly behaviours.

2. Experimental

2.1. Materials

Copper(II) bromide (CuBr$_2$, 99%), ferric chloride (FeCl$_3$, 99%), 2,2′-bipyridine (bpy, 99%), iron powder (Fe(0), 230 mesh, 99.5%), copper powder (Cu(0), 150 mesh, 99.5%), alumina (neutral), triphenylphosphine (PPh$_3$, 99%), and *N,N,N′,N″,N″*-pentamethyldiethylenetriamine (PMDETA, 99%) were purchased from Sigma-Aldrich. Ethyl α-bromoisobutyrate (EBiB, 98%), methyl methacrylate (MMA, 99%), *n*-butyl methacrylate (BMA, 99%), and benzyl methacrylate (BzMA, 99%) were purchased from TCI Co., Ltd. Proanthocyanidins (PC, 100 mesh, 80%) were provided by Compson Biotech Co., Ltd. Solvents and monomers were purified prior to use.

2.2. Iron-catalysed ATRP and chain extensions

An example of ARGET Fe-ATRP of MMA with PC as the reducing agent: a Schlenk flask was charged with MMA (4 mL, 37.6 mmol), EBiB (28 μL, 0.188 mmol), FeCl$_3$ (3 mg, 0.018 mmol), TPP (23 mg, 0.09 mmol), anisole and a desired amount of PC (MMA/EBiB/PC/FeCl$_3$/PPh$_3$ = 200/1/*x*/0.1/0.5; [MMA]$_0$ = 4.5 M). The flask was sealed and degassed through several freeze–pump–thaw cycles. An initial reference was taken and the solution was placed in a thermo stated oil bath at 60 °C. The reaction was stopped by placing into an ice bath, exposed to air, and diluted with tetrahydrofuran (THF). The solution was passed through an alumina column and precipitated in methanol. The resulting white powder of PMMA–Br was acquired. The samples were dried under vacuum and stored in a desiccator.

In a typical chain extension, BMA (1.6 mL, 10 mmol), PMMA–Br macroinitiator (MI) (M_n = 10 060 and PDI = 1.12; 0.2 g, 0.02 mmol), FeCl$_3$ (3 mg, 0.02 mmol), PPh$_3$ (21 mg, 0.08 mmol), and anisole were added to a Schlenk flask. The mixture was deoxygenated by freeze–pump–thaw cycles and backfilled with inert gas. A certain amount of PC (29 mg, 0.1 mmol) was added to the frozen solution (BMA/PMMA–Br/PC/FeCl$_3$/PPh$_3$ = 500/1/5/1/4; [BMA]$_0$ = 3 M). The solution was

kept at 90 °C and samples were withdrawn *via* a syringe at various intervals to determine the monomer conversions (*via* GC) and the MW of polymers (*via* GPC). The purification steps are the same as the steps of the above-mentioned ARGET Fe-ATRP. The resulting polymer powders were dried overnight under vacuum and the PMMA-*b*-PBMA block copolymer (BCP) (M_n = 44 740 and PDI = 1.25) was obtained.

2.3. Characterization

A PerkinElmer Spectrum One FT-IR spectrometer was utilized to analyze the absorption spectra of the cast films. Samples were dissolved in THF and the solutions were drop-cast onto a KBr disk and dried under vacuum. The monomer conversion was traced using a Hewlett–Packard gas chromatograph (GPC) equipped with a CD-5 column and an FID detector (HP 5890 ser. II). The conversion was determined based on the area (A) ratio of the monomer (M) and solvent (S) (*i.e.*, A_M/A_S) of the initial sample. ^{1}H NMR spectra were recorded using a Varian 400 NMR spectrometer. The chemical shift (δ) was calibrated to be 7.26 ppm with CDCl$_3$. A Waters gel permeation chromatography (GPC) system with a refractometer (Waters 410) and two PSS SDV columns in series (linear S and 100 Å) at 40 °C was employed (eluent: THF; flow rate: 1 mL min^{-1}). The average molecular weights M_n and M_w and the polydispersity index (PDI = M_w/M_n) were determined on the basis of polystyrene standards. Solutions with various iron complexes were degassed and sealed in a quartz Schlenk flask individually. The redox behaviors of the iron complexes were monitored using a THERMO BioMateTM 3 UV–Vis instrument. A Seiko 6220 differential scanning calorimeter (DSC) was utilized to detect the glass transition (T_g) of BCPs in the 2nd run (from 10 to 190 °C with 20 °C min^{-1} ramping rate).

The thermal stability of the BCPs was analyzed by thermogravimetric analysis (TGA) using a TA Instruments Q50 analyzer (from 50 to 700 °C under N$_{2(g)}$ with 20 °C min^{-1} ramping rate). Small-angle X-ray scattering (SAXS) was carried out using the Endstation BL23A1 of the National Synchrotron Radiation Research Center (NSRRC), Hsinchu, Taiwan. The energy of the

X-ray source and the sample-to-detector distance were 15 kV and 3 m, respectively. The *d*-spacing values were calculated from the first scattering peaks (q^*) using the formula of $d = 2\pi/q^*$. A Dimension-3100 atomic force microscope (AFM) was used at room temperature with a microcantilever (AC200TS, Olympus).

3. Results and discussion

Our "green" approach is to proceed with ATRP in the presence of higher-oxidation-state transition metals and reducing agents (RAs). Fig. 1 shows the kinetics plots of iron-based ATRP of methyl methacrylate (MMA) at 60 °C with diminishing amounts of ferric catalyst in the presence of different RAs at various concentrations (MMA/EBiB/RA/FeCl$_3$/PPh$_3$ = 200/1/*x*/0.1/0.5; *x* = 1, 5, and 10; RA = Cu(0), Fe(0), or PC) and Table 1 summarizes the corresponding reaction results. Notably, numbers in the legend in Fig. 1 correspond to the entries in Table 1. At a ratio of RA/Fe^{III} = 10/0.1 (*i.e.*, Fig. 1A), the

Table 1 Conditions for iron-catalysed SARA/ARGET ATRP and characterization

Entry^a (#)	RA	t (h)	Conv.^{a} (%)	$M_n{}^b$	PDI^c	k_{app} (×10^5 s^{-1})
1	Cu	10	72	35 000	2.14	3.50
2		6.5	84	66 340	1.75	7.75
3		12	86	17 880	1.63	4.69
4	Fe	30	41	17 460	1.31	0.348
5		9	63	27 420	1.28	2.23
6		15	73	15 620	1.44	2.54
7	PC	56	62	15 000	1.30	0.684
8		48	57	17 900	1.25	0.532
9		29	54	23 800	1.20	0.791

^{a} Molar ratios of MMA/EBiB/RA/FeCl$_3$/PPh$_3$ were 200/1/*x*/0.1/0.5; [M]$_0$ = 4.5 M in anisole; RA = reducing agent. RA/Fe^{III} = 10/0.1 in entries 1, 4, and 7. RA/Fe^{III} = 5/0.1 in entries 2, 5, and 8. RA/Fe^{III} = 1/0.1 in entries 3, 6, and 9. ^{b} Cu(0) and Fe(0): Powders with 230 mesh; PC: Powder with 100 mesh. ^{c} Values of M_n and PDI were measured by GPC (eluent: THF), with polystyrene standards for calibration.
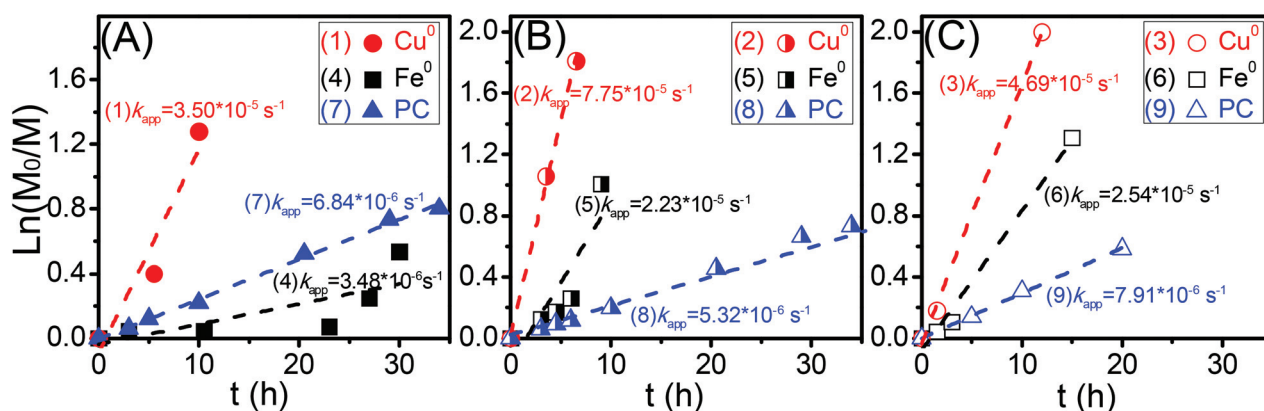

Fig. 1 Kinetics of ATRP of MMA with different reducing agents (RA) and amounts (RA/FeCl$_3$): (A) 10/0.1, (B) 5/0.1, and (C) 1/0.1 (MMA/EBiB/RA/FeCl$_3$/PPh$_3$ = 200/1/*x*/0.1/0.5 at 60 °C; [MMA]$_0$ = 4.5 M in anisole).

polymerization with Cu(0) as an RA proceeds at a much faster reaction rate (#1: $k_{app} = 3.5 \times 10^{-5}$ s^{-1}) than with Fe(0) (#4: 3.48×10^{-6} s^{-1}) and PC (#7: 6.84×10^{-6} s^{-1}) as RAs. As revealed from Table 1, the PDI of #1 (2.14) has a much higher value than those of #4 (1.31) and #7 (1.30). The large PDI value might be due to the occurrence of side reactions, such as terminations or chain transfer reactions. Similarly, as illustrated in Fig. 1B and C, polymerizations with Cu(0) exhibited fast reaction rates (#2: $k_{app} = 7.75 \times 10^{-5}$ s^{-1} and #3: $k_{app} = 4.69 \times 10^{-5}$ s^{-1}) but the PDI values were over 1.6 (shown in Table 1), indicating poor control over the reaction. Polymerization with Cu(0)/Fe(III) = 10/0.1 (i.e., #1) showed a slower reaction rate than that with Cu(0)/Fe(III) = 5/0.1 (i.e., #2). It is plausible that Cu(0) could rapidly reduce Fe(III)/PPh$_3$ and generate high concentrations of activators (i.e., Fe(II)/PPh$_3$), leading to the enhancement of terminations and a decrease of reaction rate. High PDI values were thus attained. Notably, polymerization with PC/Fe(III) = 1/0.1 (i.e., #9) proceeded at a faster reaction rate than that with PC/Fe(III) = 5/0.1 (i.e., #8). We deduce that the PC/Fe(III) ratio in #9 was insufficient to conduct effective reduction of Fe(III). Instead, Fe(III) might be partially and quickly reduced by the MMA monomer through the outer sphere electron transfer (OSET) mechanism, leading to an increase of reaction rate.[52] In summary, polymerizations with Fe(0) and PC (i.e., #6–8) proceeded at moderate reaction rates and attained rational molecular weight (MW) with low PDI values (<1.45), illustrating good control.

To further examine the efficacy of the "green" reducing agent PC on the ferric catalyst, we conducted ARGET ATRP of MMA in one case with PC and in the other case without PC. Fig. 2 shows the kinetic traces (MMA/EBiB/PC/FeCl$_3$/PPh$_3$ = 100/1/5 (or 0)/0.1/0.5 at 60 °C). As shown in Fig. 2a, we observed a pseudo-first-order reaction with a moderate reaction rate ($k_{app} = 6.34 \times 10^{-6}$ s^{-1}). In Fig. 2b, the reaction showed a similar trace to that of polymerization with PC
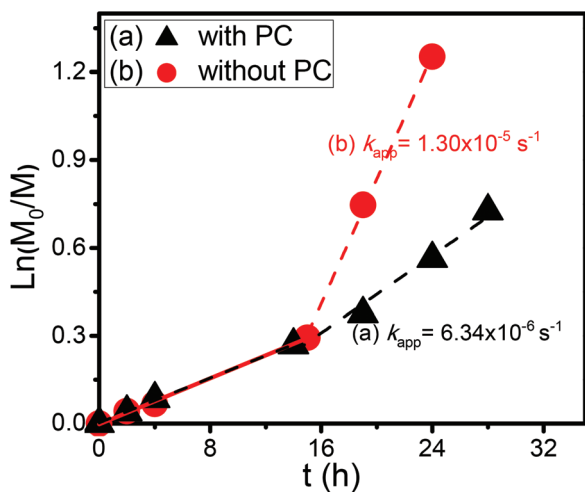
before 16 h. However, the reaction rate dramatically increased after 16 h ($k_{app} = 1.30 \times 10^{-5}$ s^{-1}). This is rationally due to the occurrence of outer sphere electron transfer (OSET) between Fe(III) and MMA, leading to the increase of the concentration of reactive species.[52] With a large ratio of MMA/FeCl$_3$ (i.e., 1000/1) and the absence of PC, the faster polymerization rate might have been resulted from the existence of high radical concentrations. The higher radical concentrations basically generate more side reactions, such as terminations and chain transfer reactions. Thus the combinations of PC/FeCl$_3$/PPh$_3$ provide an effective regulation during polymerization. In addition, we utilize PC to reduce a cupric catalyst to conduct ARGET ATRP of MMA and the results are shown in Fig. S1–S3† (MMA/EBiB/PC/CuBr$_2$/PMDETA = 500/1/5 (or 0)/0.1/1). About an order faster reaction rate was observed in the presence of PC (i.e., Fig. S1a†: $k_{app} = 6.88 \times 10^{-6}$ s^{-1}) compared to that of without PC (i.e., Fig. S1b†: $k_{app} = 6.31 \times 10^{-7}$ s^{-1}). With different ratios of MMA/EBiB (shown in Fig. S2 and S3†), living controlled fashions were clearly observed, including linear first order plots, mono-modal and linear growths of MWs (up to M_n = ca. 25 000) with low PDIs (<1.25). Notably, two experiments without degassing in one case using Cu(0) as the RA and the other one using PC as the RA were conducted (see Fig. S4 in the ESI†). We observed that the Cu(0) case showed a faster reaction rate than the PC case. It is probably because the presence of large amounts of oxygen significantly suppressed the reduction ability of PC, resulting in ineffective polymerization.

To have similar MW and PDI of macroinitiators (MIs), two ATRPs of MMA were stopped at ca. 50% conversion while in one case with and in the other case without using PC as RA (MMA/EBiB/PC/FeCl$_3$/PPh$_3$ = 200/1/5 (or 0)/0.1/0.5; [M]$_0$ = 4.5 M in anisole). Consequently, two PMMA–Br MIs were obtained (i.e., PMMA–Br$^{w\text{-}PC}$ MI: M_n = 10 060 and PDI = 1.12, and PMMA–Br$^{w'o\text{-}PC}$ MI: M_n = 10 300 and PDI = 1.17). To scrutinize the chain end fidelity, we utilize a "green" catalytic system for chain extensions of PMMA–Br MIs with MMA as shown in Fig. 3 (MMA/PMMA–Br/PC/FeCl$_3$/PPh$_3$ = 500/1/5/0.1/0.5 at
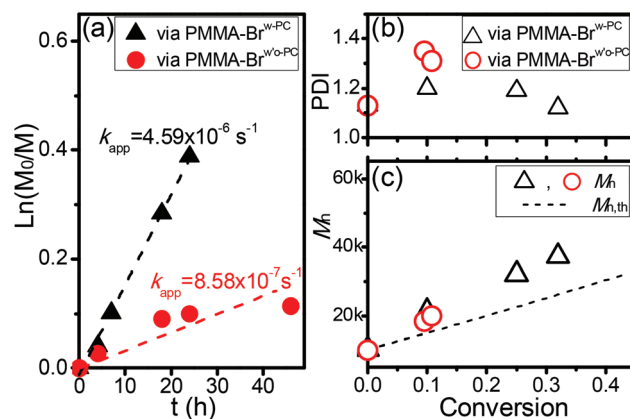

Fig. 2 Kinetics comparisons for (ARGET) ATRP of MMA at 60 °C (a) with and (b) without PC (MMA/EBiB/PC/FeCl$_3$/PPh$_3$ = 200/1/5 (or 0)/0.1/0.5; [MMA]$_0$ = 4.5 M in anisole).

Fig. 3 Kinetics plots of the chain extensions of PMMA–Br$^{w\text{-}PC}$ and PMMA–Br$^{w'o\text{-}PC}$ with MMA via ARGET ATRP ((a) first-order plot and (b/c) PDI/Mn vs. conversion plot; MMA/PMMA–Br/PC/FeCl$_3$/PPh$_3$ = 500/1/5/1/5 at 60 °C; [MMA]$_0$ = 4.5 M in anisole).
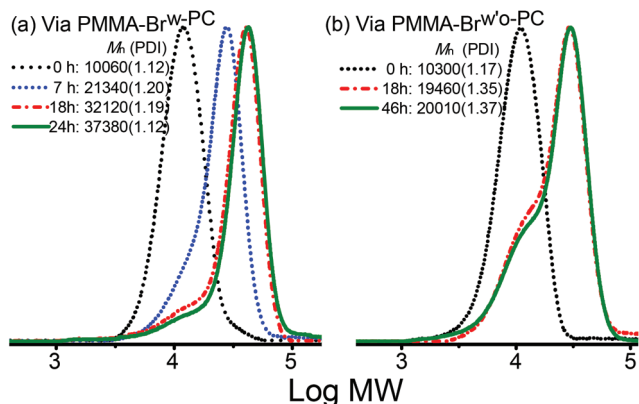
Fig. 4 GPC traces of the corresponding chain extensions of (a) PMMA–Br$^{\text{w-PC}}$ and (b) PMMA–Br$^{\text{w'o-PC}}$ with MMA in Fig. 3.

60 °C; $[\text{MMA}]_0 = 4.5$ M). In the chain extension of PMMA–Br$^{\text{w-PC}}$ (i.e., triangles in Fig. 3a–c), we attained a linear first order plot ($k_{\text{app}} = 4.59 \times 10^{-6}$ s^{-1}) and a linear growth in MWs (up to $M_n = 37\,380$) with low PDIs (<1.2). As shown in Fig. 4a, the corresponding GPC traces displayed gradual MW evolution with mono-modal traces. These results indicated a well-controlled fashion. On the other hand, we observed a pseudo-linear first order trend in the chain extension of PMMA–Br$^{\text{w'o-PC}}$ (i.e., circles in Fig. 3a–c) and low PDIs (<1.4). But the increase of M_ns was suppressed. As shown in Fig. 4b, the corresponding GPC results showed obvious bi-modal traces. These results indicated a poorly controlled manner. Hence, ATRP of MMA in the presence of PC as a reducing agent to attain the first segment of PMMA–Br properly mediated the polymerization and preserved high chain end integrity.

To comprehend the reduction ability of PC, as shown in Fig. 5, we acquire UV–Vis adsorption spectra at different times and the appearances of the FeCl$_n$/bpy systems [FeCl$_n$/bpy/PC] =
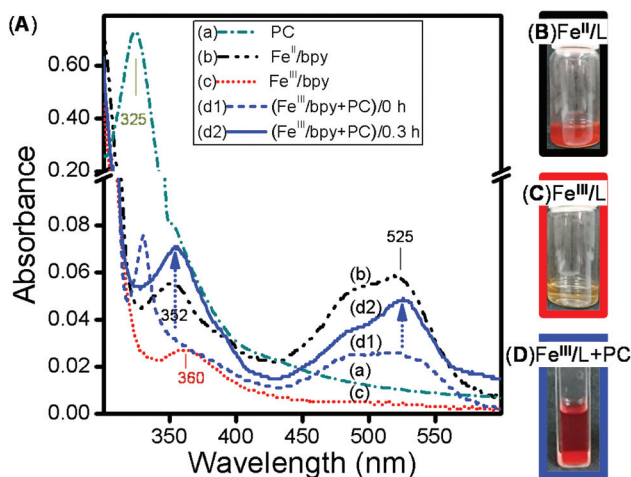
1/2/5 at 25 °C ($n = 2$ and 3); [FeCl$_n$]$_0 = 0.15$ mM]. Using bpy, we can trace the redox reactions of Fe(III) and Fe(II) in the UV/Vis region of 300–600 nm facilely and distinctively. Following the reference traces (i.e., the curves a–c in Fig. 2a), the (a) PC (dashed-dotted line), (b) Fe$^{\text{II}}$/bpy (dashed-dotted-dotted line), and (c) Fe$^{\text{III}}$/bpy (dotted line) compounds show relatively significant absorption signals at ca. (a) 325, (b) 352/525, and (c) 360 nm, respectively. Upon adding PC to the FeCl$_3$/bpy complex (i.e., dashed line d1 in Fig. 5A), a strong peak from PC and minor peaks from iron complexes were observed. Notably, the intensity at ca. 525 nm was obvious at the initial time (i.e., 0 h), indicating a fast reduction behavior. After reducing for 0.3 h (i.e., solid line d2 in Fig. 5A), we observed a significant decrease at 325 nm and increases at 352 and 525 nm with an observable isosbestic point at 334 nm. Corresponding to Fig. 5B–D, the mixture of Fe$^{\text{III}}$/bpy and PC (i.e., 5D) became purple-pink in color in the presence of PC. These results illustrated that reductions of higher-oxidation-state complexes can be effectively attained with PC.

Subsequently, chain extensions (C.E.) of PMMA–Br$^{\text{w-PC}}$ with MMA, n-butyl methacrylate (BMA), and benzyl methacrylate (BzMA) monomers (M) were conducted (M/PMMA–Br/PC/FeCl$_3$/PPh$_3$ = 500/1/5/1/5; [M]$_0$ = 3 M in anisole). As shown in Fig. 6, gradual increase of MWs (up to $M_n = 46\,000$) with low PDIs (<1.45) was observed. We then analysed the chemical structures of these polymers using a ^{1}H NMR spectrometer (400 MHz, CDCl$_3$). As shown in Fig. 7A, typical PMMA signals were acquired (i.e., peaks a–d). Notably, the chain end signal of the resulted PMMA–PMMA–Br (i.e., peak e) was still attained, providing the evidence of living polymer chains. In the spectrum of PMMA-b-PBMA (i.e., Fig. 7B), both signals of PMMA and PBMA were acquired. From the area ratio of c (3.69 ppm) and d' (3.89 ppm), a PMMA$_{100}$-b-PBMA$_{537}$ block copolymer (BCP) was obtained (i.e., (A_c/3H) : ($A_{d'}$/2H) = 1 : 5.37). In the spectrum of PMMA-b-PBzMA (i.e., Fig. 7C), signals of PMMA and PBzMA were also acquired. From the area ratio of c (3.69 ppm) and d″ (4.89 ppm), a PMMA$_{100}$-b-PBzMA$_{649}$ BCP
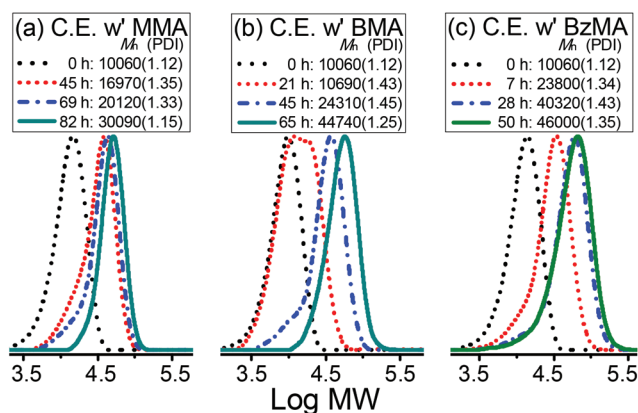

Fig. 5 (A) UV–Vis adsorption spectra of various iron complexes in MeCN ([FeCl$_n$/bpy/PC] = 1/2/5 at 25 °C; [FeCl$_n$]$_0 = 0.15$ mM; $n = 2$ or 3; L = bpy). Solution images of (B) Fe$^{\text{II}}$/L, (C) Fe$^{\text{III}}$/L, and (D) (Fe$^{\text{III}}$/L+PC).

Fig. 6 GPC traces of the chain extensions (C.E.) of PMMA–Br with (a) MMA, (b) BMA, and (c) BzMA (M/PMMA–Br/PC/FeCl$_3$/PPh$_3$ = 500/1/5/1/4; [M]$_0$ = 3 M in anisole).
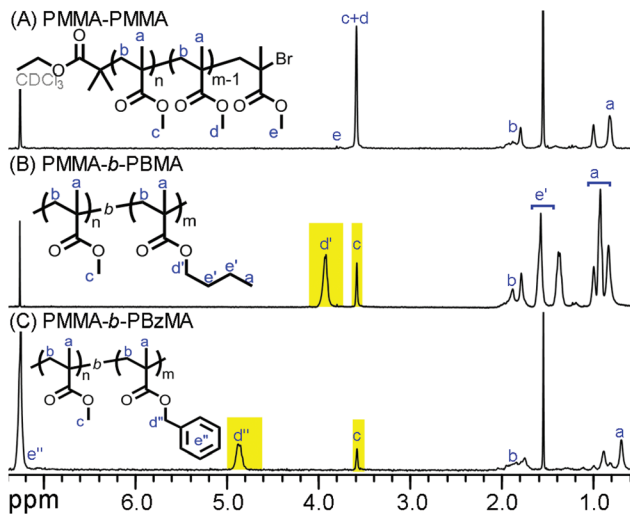
Fig. 7 ^{1}H NMR (400 MHz, CDCl$_3$) spectra of (A) PMMA–PMMA (B) PMMA-*b*-PBMA, and (C) PMMA-*b*-PBzMA (co)polymers.

was obtained (*i.e.*, $(A_c/3H):(A_{d''}/2H) = 1:6.49$). Fig. S5† shows the analysis of the FT-IR spectra of the obtained BCPs ((a) PMMA-*b*-PBzMA and (b) PMMA-*b*-PBMA in the range of 4000–400 cm^{-1}). Well-defined polymers, including a homopolymer of PMMA–PMMA and two BCPs of PMMA-*b*-PBMA and PMMA-*b*-PBzMA were thus obtained.

Thermal stability of the BCPs was examined by thermogravimetric analysis (TGA) under a N$_{2(g)}$ atmosphere. As displayed in Fig. 8, PMMA$_{100}$-*b*-PBzMA$_{649}$ (curve a) shows single-step pyrolysis with a maximum decomposition rate (r_d) at *ca.* 330 °C. The thermal properties of 5 wt% decomposition ($T_{d5\%}$) and the char yield were about 250 °C and 0.9 wt%, respectively. The PMMA$_{100}$-*b*-PBMA$_{537}$ (curve b) shows a similar profile and the r_d, $T_{d5\%}$ and char yield were approximately 350 °C, 270 °C, and 3.9 wt%, respectively. Fig. 9 displays differential scanning
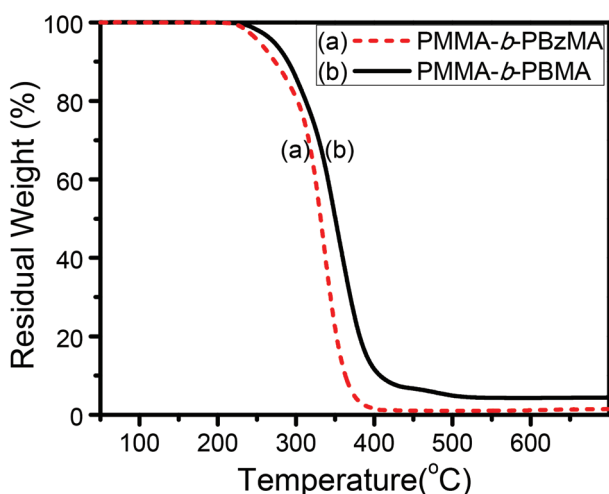

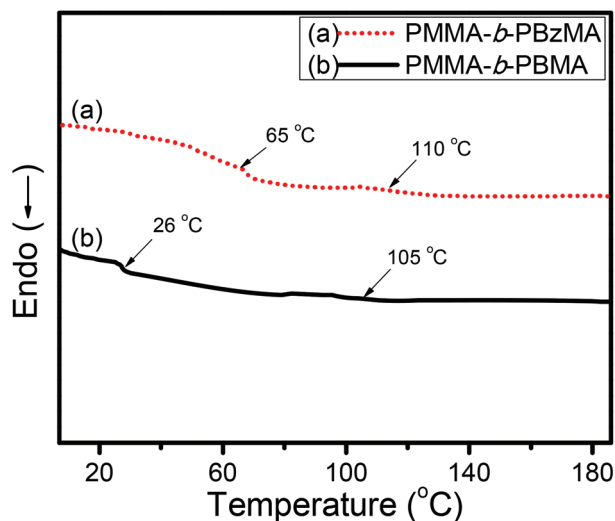**Fig. 8** TGA curves of (a) PMMA$_{100}$-*b*-PBzMA$_{649}$ and (b) PMMA$_{100}$-*b*-PBMA$_{537}$.

Fig. 9 DSC traces of (a) PMMA$_{100}$-*b*-PBzMA$_{649}$ and (b) PMMA$_{100}$-*b*-PBMA$_{537}$.

calorimetry (DSC) traces of the corresponding BCPs. T_gs of the pristine PBMA, PBzMA, and PMMA homopolymers are approximately 20, 54, and 105 °C, respectively. In the PMMA$_{100}$-*b*-PBzMA$_{649}$ BCP (*i.e.*, Fig. 9a), two T_gs of approximately 63 and 110 °C, corresponding to the segments of PBzMA and PMMA, are observed. For the PMMA segment, we obtained a slight T_g increase (+5 °C) compared to the pristine PMMA homopolymer. The increase basically comes from the decrease in the mobility of the PMMA segment which might be due to the restraint from the benzene rings of PBzMA. For the PBzMA segment, a significant T_g increase was acquired (+11 °C), indicating a moderate compatibility between PBzMA and PMMA segments. In PMMA$_{100}$-*b*-PBMA$_{537}$ BCP (*i.e.*, Fig. 9b), we also observed two T_gs of 26 and 105 °C, corresponding to the segments of PBMA and PMMA. Notably, the T_gs of each segment did not show significant shifts. Compared to pristine homopolymers, it is known that the resulting T_g differences (*i.e.*, ΔT_g) of block copolymers or polymer blends can rationally reflect the miscibility of the components. The higher ΔT_g value generally illustrates a less compatible system. We then compared the T_g difference of BCP from each segment (*i.e.*, $\Delta T_{g(BCP)}$) and T_g difference of the corresponding pristine homopolymers ($\Delta T_{g(homos)}$). As shown in Table 2, the $\Delta T_{g(BCP)}/\Delta T_{g(homos)}$ of PMMA-*b*-PBMA has a larger value (0.93)

Table 2 Thermal properties of the BCPs

Sample	$r_d{}^a$ (°C)	$T_{d5\%}{}^b$ (°C)	Char yield (%)	T_g (°C)	$\Delta T_{g(BCP)}/$ $\Delta T_{g(homos)}{}^c$
PMMA-*b*-PBzMA	330	250	0.9	65, 110	0.78
PMMA-*b*-PBMA	350	270	3.9	26, 105	0.93

^{a} From the maximum slope of the decomposition curves. ^{b} The temperatures at 5 wt% decomposition of the BCPs. ^{c} $\Delta T_{g(BCP)}$: T_g difference of the BCP from each segment measured by DSC; $\Delta T_{g(homos)}$: T_g difference of pristine homopolymers.

than that of the PMMA-*b*-PBzMA (0.78), indicating a highly incompatible system of PMMA-*b*-PBMA. The TGA and DSC results are summarized in Table 2.

We then investigate the self-assembly properties of the PMMA-*b*-PBzMA and PMMA-*b*-PBMA. Polymer mixtures most likely become less miscible as the temperature decreases. Due to the covalent linkage between BCP segments, namely, most BCP systems exhibit upper critical ordering temperatures (UCOT) which are similar to the phenomenon of upper critical solution temperature (UCST) in polymer solutions. Below the UCOT, phase separation occurs. Fig. 10 shows dynamic one-dimensional small-angle X-ray scattering (1D SAXS) intensity tracing of (A) PMMA-*b*-PBzMA and (B) PMMA-*b*-PBMA with increasing temperatures. Obviously, PMMA-*b*-PBzMA was disordered throughout the experimental temperature range (Fig. 10A); by contrast, PMMA-*b*-PBMA exhibited an apparent UCOT. As shown in Fig. 10B, a UCOT could be observed between 125 and 140 °C for a PMMA-*b*-PBMA testing sample. As mentioned above, the ΔT_g(BCP)/ΔT_g(homos) of the PMMA-*b*-PBMA has a larger value than that of the PMMA-*b*-PBzMA, indicating a highly incompatible system of PMMA-*b*-PBMA. Namely, PMMA-*b*-PBMA BCPs possessed a stronger tendency to phase separate, leading to distinct UCOT characteristics. The variation of scattering intensity might be caused by the thermally induced volume changes of the testing samples.

Static 1D SAXS profiles of the isotherm at 30 and 150 °C were obtain to confirm their phase separation behaviors. It is noted that the functional groups of the synthesized polymer chains were similar so that staining by volatile rare transition metal oxides (*e.g.*, RuO$_4$) was difficult to bring out imaging contrast under transmission electron microscopy (TEM) observation. Therefore, atomic force microscopy (AFM) was conducted for identification of self-assembled morphologies.
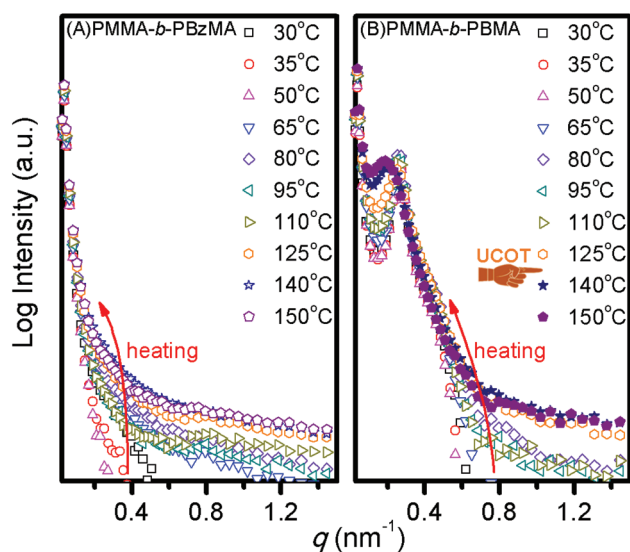
Thin-film samples were prepared on clean glass substrates by spin-coating at 3000 rpm for 1 min using 1 wt% toluene solutions of the synthesized BCPs. As expected, the 1D SAXS profiles of the PMMA-*b*-PBzMA (*i.e.*, Fig. 11a) showed insignificant reflections at both temperatures and the corresponding AFM phase image (*i.e.*, Fig. 11b) also showed a blurred morphology without distinctive phase separation. As shown in Fig. 11c, by contrast, the 1D SAXS profile of the PMMA-*b*-PBMA at 30 °C confirms a sphere packed into BCC unit cells with a space group of $Im\bar{3}m$ at which scattering peaks are found with a series of $q^* : \sqrt{3}q^* : \sqrt{4}q^* : \sqrt{5}q^*$ (q^* = 0.2608 nm^{-1}). The allowed reflections for a body-centered cubic (BCC) lattice arise from the (110), (200), (211), (220), and (310) planes. The interdomain spacing between the BCC microdomains (d_{BCC}) was calculated to be around 24 nm. When the sample was kept at 150 °C, disappearance of the ordering was observed that resulted from the above-mentioned UCOT behaviour. Evident self-assembled spherical morphologies could also be identified by AFM (Fig. 11d). The phase contrast is related to the material stiffness. In the previous DSC results, the T_gs of PMMA and PBMA were 105 and 26 °C, respectively, indicating that PMMA was in the glassy state while PBMA was in a rubber-
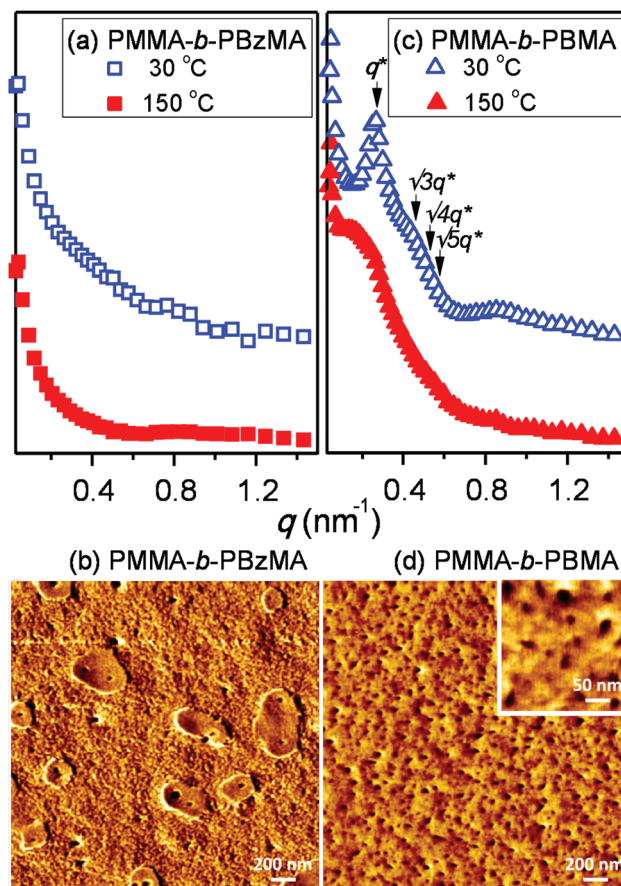

Fig. 11 SAXS intensity profiles of (a) PMMA-*b*-PBzMA (squares) and (c) PMMA-*b*-PBMA (triangles) at 30 (open symbols) and 150 °C (solid symbols). Tapping-mode AFM phase images of the morphologies of (b) PMMA-*b*-PBzMA and (d) PMMA-*b*-PBMA.

Fig. 10 SAXS intensity traces with increasing temperatures for (A) PMMA-*b*-PBzMA and (B) PMMA-*b*-PBMA (UCOT: upper critical ordering temperature).

like state at room temperature. Consequently, the darker areas in the phase image could be attributed to the stiff PMMA matrix and the brighter areas belonged to softer PBMA domains. The sphere diameter was around 30 nm. The results of 1D SAXS and AFM measurements revealed that PMMA-*b*-PBMA possessed a stronger tendency to self-assemble into microdomains, which was in agreement with the volume fraction of BCP (f_{PMMA} = 11.4%).

4. Conclusions

Iron(III)-catalysed ATRPs of MMA were conducted with various reducing agents Cu(0), Fe(0), and PC. From the kinetics analysis results, Fe(0) and PC provided moderate reaction rates resulting in PMMA–Br with low PDIs (<1.45). On further conducting chain extensions of MMA, a linear first order reaction (k_{app} = 4.59 × 10^{-6} s^{-1}) and a linear increase in MWs (up to M_n = 37 380) with low PDIs (<1.2) were attained. The efficacy of catalyst reduction using PC was revealed using an UV–Vis adsorption spectrometer. We thus carried out chain extensions of BzMA and BMA in the presence of PC and then obtained well-defined BCPs of PMMA$_{100}$-*b*-PBzMA$_{649}$ (PDI = 1.35) and PMMA$_{100}$-*b*-PBMA$_{537}$ (PDI = 1.25). From the DSC results, the PMMA-*b*-PBMA shows less segmental compatibility than PMMA-*b*-PBzMA. As revealed by SAXS and AFM, PMMA-*b*-PBzMA displayed a disordered morphology. In the case of PMMA-*b*-PBMA, we observed an UCOT behaviour and acquired a typically self-assembled spherical morphology with an interdomain spacing of around 25 nm. Herein, we demonstrated an effective environmentally friendly iron-catalyzed ATRP using a natural product PC to synthesize polymethacrylate-based BCPs. Fabrications of diverse microstructures, such as A15 phase, are currently underway.

Conflicts of interest

There are no conflicts to declare.

Acknowledgements

References

1 M. Kamigaito, T. Ando and M. Sawamoto, *Chem. Rev.*, 2001, **101**, 3689–3745.

2 J. S. Wang and K. Matyjaszewski, *J. Am. Chem. Soc.*, 1995, **117**, 5614–5615.

3 Y.-S. Huang, J.-K. Chen, T. Chen and C.-F. Huang, *Polymers*, 2017, **9**, 231.

4 J. Chiefari, Y. K. Chong, F. Ercole, J. Krstina, J. Jeffery, T. P. T. Le, R. T. A. Mayadunne, G. F. Meijs, C. L. Moad, G. Moad, E. Rizzardo and S. H. Thang, *Macromolecules*, 1998, **31**, 5559–5562.

5 M. Destarac, *Polym. Chem.*, 2018, **9**, 4947–4967.

6 C. J. Hawker, A. W. Bosman and E. Harth, *Chem. Rev.*, 2001, **101**, 3661–3688.

7 C.-F. Huang, W.-H. Chen, J. Aimi, Y.-S. Huang, S. Venkatesan, Y.-W. Chiang, S.-H. Huang, S.-W. Kuo and T. Chen, *Polym. Chem.*, 2018, **9**, 5644–5654.

8 J. Aimi, P.-H. Wang, C.-C. Shih, C.-F. Huang, T. Nakanishi, M. Takeuchi, H.-Y. Hsuehe and W.-C. Chen, *J. Mater. Chem. C*, 2018, **6**, 2724–2732.

9 C. F. Huang, J. Aimi and K. Y. Lai, *Macromol. Rapid Commun.*, 2017, **38**, 1600607.

10 J.-K. Chen, C.-Y. Hsieh, C.-F. Huang and P.-M. Li, *J. Colloid Interface Sci.*, 2009, **338**, 428–434.

11 T. Hirai, M. Kobayashi and A. Takahara, *Polym. Chem.*, 2017, **8**, 5456–5468.

12 W. Tang, Y. Kwak, W. Braunecker, N. V. Tsarevsky, M. L. Coote and K. Matyjaszewski, *J. Am. Chem. Soc.*, 2008, **130**, 10702–10713.

13 W. Tang, N. V. Tsarevsky and K. Matyjaszewski, *J. Am. Chem. Soc.*, 2006, **128**, 1598–1604.

14 P. Chmielarz, M. Fantin, S. Park, A. A. Isse, A. Gennaro, A. J. D. Magenau, A. Sobkowiak and K. Matyjaszewski, *Prog. Polym. Sci.*, 2017, **69**, 47–78.

15 A. J. D. Magenau, N. C. Strandwitz, A. Gennaro and K. Matyjaszewski, *Science*, 2011, **332**, 81–84.

16 S. Park, P. Chmielarz, A. Gennaro and K. Matyjaszewski, *Angew. Chem., Int. Ed.*, 2015, **54**, 2388–2392.

17 G. Yilmaz and Y. Yagci, *Polym. Chem.*, 2018, **9**, 1757–1762.

18 G. R. Jones, R. Whitfield, A. Anastasaki and D. M. Haddleton, *J. Am. Chem. Soc.*, 2016, **138**, 7346–7352.

19 X. C. Pan, N. Malhotra, A. Simakova, Z. Y. Wang, D. Konkolewicz and K. Matyjaszewski, *J. Am. Chem. Soc.*, 2015, **137**, 15430–15433.

20 Y. N. Zhou, J. J. Li, D. Ljubic, Z. H. Luo and S. P. Zhu, *Macromolecules*, 2018, **51**, 6911–6921.

21 Z. H. Wang, X. C. Pan, J. J. Yan, S. Dadashi-Silab, G. J. Xie, J. N. Zhang, Z. H. Wang, H. S. Xia and K. Matyjaszewski, *ACS Macro Lett.*, 2017, **6**, 546–549.

22 Z. H. Wang, Z. H. Wang, X. C. Pan, L. Y. Fu, S. Lathwal, M. Olszewski, J. J. Yan, A. E. Enciso, Z. Y. Wang, H. S. Xia and K. Matyjaszewski, *ACS Macro Lett.*, 2018, **7**, 275–280.

23 I. Zaborniak and P. Chmielarz, *Materials*, 2019, **12**, 3600.

24 W. Jakubowski and K. Matyjaszewski, *Angew. Chem., Int. Ed.*, 2006, **45**, 4482–4486.

25 L. Quiros-Montes, G. A. Carriedo, J. Garcia-Alvarez and A. P. Soto, *Green Chem.*, 2019, **21**, 5865–5875.

26 K. Matyjaszewski, W. Jakubowski, K. Min, W. Tang, J. Y. Huang, W. A. Braunecker and N. V. Tsarevsky, *Proc. Natl. Acad. Sci. U. S. A.*, 2006, **103**, 15309–15314.

27 Y. Z. Zhang, Y. Wang and K. Matyjaszewski, *Macromolecules*, 2011, **44**, 683–685.

28 K. Borska, D. Moravcikova and J. Mosnacek, *Macromol. Rapid Commun.*, 2017, **38**, 1600639.

29 J. Mosnacek and M. Ilcikova, *Macromolecules*, 2012, **45**, 5859–5865.

30 A. Simakova, M. Mackenzie, S. E. Averick, S. Park and K. Matyjaszewski, *Angew. Chem., Int. Ed.*, 2013, **52**, 12148–12151.

31 L. F. Zhang, Z. P. Cheng, F. Tang, Q. Li and X. L. Zhu, *Macromol. Chem. Phys.*, 2008, **209**, 1705–1713.

32 L. F. Zhang, Z. P. Cheng, Y. T. Lu and X. L. Zhu, *Macromol. Rapid Commun.*, 2009, **30**, 543–547.

33 L. F. Zhang, Z. P. Cheng, Z. B. Zhang, D. Y. Xu and X. L. Zhu, *Polym. Bull.*, 2010, **64**, 233–244.

34 J. L. Pan, Z. Li, L. F. Zhang, Z. P. Cheng and X. L. Zhu, *Chin. J. Polym. Sci.*, 2014, **32**, 1010–1018.

35 Y. Wang, Y. Z. Zhang, B. Parker and K. Matyjaszewski, *Macromolecules*, 2011, **44**, 4022–4025.

36 K. Mukumoto, Y. Wang and K. Matyjaszewski, *ACS Macro Lett.*, 2012, **1**, 599–602.

37 S. Okada, S. Park and K. Matyjaszewski, *ACS Macro Lett.*, 2014, **3**, 944–947.

38 G. H. Zhu, L. F. Zhang, Z. B. Zhang, J. Zhu, Y. F. Tu, Z. P. Cheng and X. L. Zhu, *Macromolecules*, 2011, **44**, 3233–3239.

39 J. Wu, X. W. Jiang, L. F. Zhang, Z. P. Cheng and X. L. Zhu, *Polymers*, 2016, **8**, 29.

40 X. C. Pan, N. Malhotra, J. N. Zhang and K. Matyjaszewski, *Macromolecules*, 2015, **48**, 6948–6954.

41 Z. G. Xue, J. Zhou, D. He, F. Wu, D. F. Yang, Y. S. Ye, Y. G. Liao, X. P. Zhou and X. L. Xie, *Dalton Trans.*, 2014, **43**, 16528–16533.

42 J. Wu, B. J. Zhang, L. F. Zhang, Z. P. Cheng and X. L. Zhu, *Macromol. Rapid Commun.*, 2017, **38**, 1700116.

43 R. Luo and A. Sen, *Macromolecules*, 2008, **41**, 4514–4518.

44 K. Matyjaszewski, M. L. Wei, J. H. Xia and N. E. McDermott, *Macromolecules*, 1997, **30**, 8161–8164.

45 T. Ando, M. Kamigaito and M. Sawamoto, *Macromolecules*, 1997, **30**, 4507–4510.

46 C.-F. Huang, Y.-A. Hsieh, S.-C. Hsu and K. Matyjaszewski, *Polymer*, 2014, **55**, 6051–6057.

47 C.-F. Huang, R. Nicolay, Y. Kwak, F.-C. Chang and K. Matyjaszewski, *Macromolecules*, 2009, **42**, 8198–8210.

48 C.-F. Huang, S.-W. Kuo, H.-F. Lee and F.-C. Chang, *Polymer*, 2005, **46**, 1561–1565.

49 Y. Yagci and M. Atilla Tasdelen, *Prog. Polym. Sci.*, 2006, **31**, 1133–1170.

50 D. Y. Zhao, J. L. Feng, Q. S. Huo, N. Melosh, G. H. Fredrickson, B. F. Chmelka and G. D. Stucky, *Science*, 1998, **279**, 548–552.

51 H. Y. Jung and M. J. Park, *Soft Matter*, 2017, **13**, 250–257.

52 A. K. Nanda, S. C. Hong and K. Matyjaszewski, *Macromol. Chem. Phys.*, 2003, **204**, 1151–1159.